Carbohydrate Polymers 233 (2020) 115838

Contents lists available at ScienceDirect

Carbohydrate Polymers

journal homepage: www.elsevier.com/locate/carbpol

Facile synthesis of TiO_2/CNC nanocomposites for enhanced Cr(VI) photoreduction: Synergistic roles of cellulose nanocrystals

Yanxiang Li[a], Jinju Zhang[a], Chengbo Zhan[b], Fangong Kong[c], Wangliang Li[a,*], Chuanfang Yang[a,*], Benjamin S. Hsiao[b,*]

[a] CAS Key Laboratory of Green Process and Engineering, Institute of Process Engineering, Chinese Academy of Sciences, Beijing, 100190, China
[b] Department of Chemistry, Stony Brook University, Stony Brook, NY 11794, United States
[c] Key Laboratory of Pulp and Paper Science & Technology of Ministry of Education/Shandong Province, Qilu University of Technology, Jinan, 250353, China

ARTICLE INFO

Keywords:
Cellulose nanocrystals
TiO_2
Cr(VI) photoreduction
Ligand-to-metal charge transfer
Green synthesis

ABSTRACT

In this study, TiO_2 nanocrystals were synthesized in the scaffold of cellulose nanocrystal (CNC) using *in situ* hydrolysis, where the morphology and size of TiO_2 was controlled by CNC's functional groups and surface charge. The resulting TiO_2/CNC nanocomposites showed a superior photocatalytic activity for Cr(VI) reduction under visible light ($\lambda > 420$ nm) due to the combined effects of small TiO_2 size and ligand-to-metal charge transfer (LMCT) complex between CNC and TiO_2. It was found that the charge-enriched CNC not only acted as a template to direct the crystal growth of TiO_2, but also played essential roles on light harvesting and charge transfer thereby promoting the photoreduction of Cr(VI). The demonstrated system represents a unique pathway to develop a lower cost and efficient purification material for remediation of Cr(VI).

1. Introduction

Hexavalent chromium ion Cr(VI) is one of the most toxic metal ions due to its mutagenic and carcinogenic effects on biological systems and living organisms (Owlad, Aroua, Daud, & Baroutian, 2009; Zhitkovich, 2011). The accidental discharge of Cr(VI) from industries into water sources can cause serious environmental and health problems. As a result, many techniques have been developed to remove Cr(VI) from drinking water, where the maximum tolerance level is set at 0.05 mg/L. The existing methods, such as ion exchange, chemical precipitation, membrane separation and adsorption, although widely used, still have some limitations, ranging from low efficiency, secondary contamination to high operating costs (Barrera-Díaz, Lugo-Lugo, & Bilyeu, 2012). Within these methods, the adsorption approach is the most attractive one as it is capable of removing low concentrations of Cr(VI) with good efficiency (Li, Li, Cao, & Yang, 2015; Lu, Xu, Yang, Hao, & Cheng, 2017; Makhado, Pandey, & Ramontja, 2019; Mei, Zhang, Li, & Ou, 2019; Wu, Wei, & Zhang, 2012). However, the adsorbents are easily saturated and the adsorbates can form secondary contaminants and they need to be remediated (the adsorbates are usually difficult to be converted into environmental-friendly substances). One way to deal with this problem is to covert Cr(VI) first into less harmful Cr(III) by reduction, where Cr (III) can be further converted into $Cr(OH)_3$ (at pH ≥ 7) that can precipitate and be removed as a solid waste (Li, Bian, Qin, Zhang, & Bian, 2017; Loloei, Rezaee, Roohaghdam, & Aliofkhazraei, 2017).

Among the reduction techniques, the photocatalytic reduction method is most commonly considered in water purification as it utilizes the clean and renewable energy from sunlight (Acharya, Naik, & Parida, 2018; Kazemi, Jahanshahi, & Peyravi, 2018; Li et al., 2017; Pelaez et al., 2012; Zhang, Xu, Li, Ge, & Bian, 2018). In photocatalysis applications, titanium dioxide (TiO_2) nanomaterials, due to their remarkable properties of low-cost, non-toxicity and high stability, have attracted a great deal of interests as they are very suitable for environmental remediation and solar energy conversion.(Chen & Mao, 2007; Pelaez et al., 2012) The photocatalytic activity of TiO_2 is mainly dependent on the crystalline structure and specific surface area, where the larger content of anatase phase and greater surface area often lead to higher efficiency (Odling & Robertson, 2015). However, nanosized TiO_2 particles also display tendency to agglomerate and lose some effective surface area, and they are difficult to recover, which pose major challenges for their applications. One effective strategy to address this issue is to immobilize TiO_2 nanoparticles in a suitable scaffold, such as biomass derived cellulose (Li, Cao, Li, & Yang, 2015; Mohamed et al., 2015; Zhao et al., 2011). Due to the abundant hydroxyl groups on the cellulose surface, its scaffold can act as a biotemplate to direct the growth of TiO_2 nanocrystals. Inspired by these studies, we have

* Corresponding authors.
E-mail addresses: wlli@ipe.ac.cn (W. Li), cfyang@ipe.ac.cn (C. Yang), benjamin.hsiao@stonybrook.edu (B.S. Hsiao).

https://doi.org/10.1016/j.carbpol.2020.115838
Received 1 October 2019; Received in revised form 2 December 2019; Accepted 6 January 2020
Available online 11 January 2020
0144-8617/

investigated the use of nanoscale cellulose as a possible scaffold to immobilize TiO_2 nanoparticles through *in situ* growth process. The chosen nanocellulose was cellulose nanocrystal (CNC), consisting of rod-like cellulose crystals (width: 5–10 nm, length: 100–500 nm), which were produced by removing the amorphous portions of a purified cellulose source through acid hydrolysis. CNC possesses unique features including large surface area, good mechanical strength, and negatively charged sulfuric groups (besides hydroxyl groups on the cellulose surface) (Grishkewich, Mohammed, Tang, & Tam, 2017; Klemm et al., 2011; Mondal, 2017; Tang, Sisler, Grishkewich, & Tam, 2017). CNC has been demonstrated as a good scaffold to host the formation of varying nanoparticles, including TiO_2 (Kaushik & Moores, 2016; Wu et al., 2016). For example, Zhou, Ding, & Li (2007) reported the CNC-template synthesis of TiO_2 nanocubes by hydrolysis of titanium chloride ($TiCl_4$) at 95 °C. It is known that $TiCl_4$ was not easy to handle due to the fast hydrolysis rate, so the resulted particle size was relatively large (about 200 nm). However, the growth mechanism of TiO_2 and the application of the final composites were not investigated in this study. Ivanova et al. (Ivanova, Fattakhova-Rohlfing, Kayaalp, Rathouský, & Bein, 2014; Xue et al., 2017) reported the mesoporous TiO_2 through biotemplating with the CNC scaffold, in which CNC provided confined space for the controlled growth of TiO_2 crystals and created mesopores after CNC being removed by calcination. The demonstrated mesoporous TiO_2 material showed efficient photocatalytic activity.

Regarding the photocatalysis of TiO_2, there are several issues that can limit its utilization, where the major challenge is the wide band gap under visible light. The most popular methods to extend its optical response to the visible light region are doping (Asahi, Morikawa, Ohwaki, Aoki, & Taga, 2001) and dye-sensitization (O'Regan & Grätzel, 1991). Typically, the doping of foreign elements into the TiO_2 lattice requires the use of energy intensive process, such as high temperature annealing or hydrothermal treatment. In dye-sensitization, the dye molecules should generate photoexcited electrons upon irradiation, where electrons are transferred to the conduction band of TiO_2. The major requirement for dye-sensitization to be practical is that the dye molecules must be very stable in an aqueous environment. As a result, most sensitizers are limited to bipyridyl complexes, often containing expensive and toxic metals such as ruthenium. The ligand-to-metal charge transfer (LMCT) complex is another type of sensitization (Zhang, Kim, & Choi, 2014). Unlike dye sensitization, the visible light-induced charge transfer occurs from the complex's surface rather than by absorbing the visible light by sensitizer itself. So a wide variety of compounds (that do not absorb visible light) are potential candidates for sensitizers. So far, tartaric, citric and lactic acids (Wang et al., 2010), glucose (Kim, Lee, & Choi, 2015), dopamine (Kim et al., 2017), algea (Wang, Zhang, Gao, Mailhot, & Pan, 2017), carboxylate-rich porous carbon (Qu et al., 2015) and polymeric poly(4-vinylphenol) (Zhang, Kim, & Choi, 2017), etc. have all been reported to induce CT-complexation on TiO_2. In particular, as carboxylate and hydroxyl groups are rich in electrons, they have become the most popular functional groups to induce the LMCT and extend the light response of TiO_2 to the visible region. Since CNC possesses both electron-rich hydroxyl and sulfuric groups, we speculate that it is promising material to form visible light active CT-complexes with TiO_2.

Considering the potential aggregation and recovery issues, as well as the low solar energy utilization, the development of new visible-light-driven TiO_2 photocatalytic materials with high efficiency has become a particularly interesting topic to us. In this work, a facile *in situ* hydrolysis and CNC-templated approach was used to synthesize TiO_2/CNC nanocomposites with anatase TiO_2 crystals and large specific surface areas. CNC can serve not only as a supporting scaffold with directed templating capability, but also provide LMCT-forming ligands due to the electron-rich hydroxyl and sulfuric groups. The functional groups, especially those with negative charges, were found to be able to control the size and morphology of TiO_2 nanoparticles on the CNC surface. It was interesting to find that the resulting TiO_2/CNC nanocomposite can initiate the photoreduction of Cr(VI) into Cr(III) with visible light, without the need to remove the template by high-temperature calcination. In addition, the negatively charged CNC scaffold can be used to adsorb the positively charged Cr(III) ions. Compared with other Cr(VI) removal techniques, such as the common hydrothermal method, the demonstrated biotemplate mediated method involving the *in situ* growth of TiO_2 in a CNC scaffold represents a very low-cost and energy-saving remediation pathway.

2. Experimental

2.1. Materials

Cellulose nanocrystals (CNC) were supplied by the InnoTech Alberta in Canada, the sulfur content of CNC was 0.831 wt%. Titanium oxysulfate solution ($TiOSO_4 \cdot H_2SO_4 \cdot H_2O$, ~15 wt % in dilute sulfuric acid) and potassium dichromate ($K_2Cr_2O_7$) were purchased from Aldrich. All chemicals were analytical grade and used as received. The commercial nanostructured TiO_2 photoreduction agent (P25) with particle size about 21 nm was obtained from Sigma-Aldrich.

2.2. Synthesis of TiO_2/CNC nanocomposites

The typical synthesis procedure for making TiO_2/CNC nanocomposites is as follows. A CNC suspension was prepared by dispersing 0.2 g of CNC powder in 200 mL distilled water, followed by using the ultrasonic treatment to obtain a well-dispersed aqueous suspension. A desired amount of $TiOSO_4 \cdot H_2SO_4 \cdot H_2O$ with a concentration of 0.48 mol/L was then added to the CNC suspension. The mixture was kept under stirring at 70 °C. The resulting TiO_2/CNC suspension was centrifuged, washed with distilled water, and freeze-dried to obtain TiO_2/CNC composite. The chosen synthesis parameters are listed in Table S1 in *Supporting Information*. For comparison, pristine TiO_2 nanoparticles were also prepared under the same conditions without the presence of CNC.

In order to investigate the effects of surface charge and functional groups on CNC on the growth of TiO_2, desulfated CNC was used. Desulfation of CNC was carried out using the procedure reported in the literature.(Cherhal, Cousin, & Capron, 2015; Kalashnikova, Bizot, Cathala, & Capron, 2012) Subsequent carboxylation of desulfated CNC (*d*-CNC) was carried out to obtain carboxylated *d*-CNC (*c*-CNC) according to the reported TEMPO-mediated method (Guo et al., 2017) (TEM images of CNC, *d*-CNC and *c*-CNC are shown in Fig. S1, *Supporting Information*). The scaffolds of *d*-CNC and *c*-CNC were also used as the templates to synthesize TiO_2/*d*-CNC and TiO_2/*c*-CNC nanocomposites, respectively, under the same conditions as for TiO_2/CNC.

2.3. Characterization

The surface morphology of the TiO_2/CNC nanocomposite was analyzed by using a scanning electron microscope (SEM, SFEG-SEM LEO1550) with Robinson backscattered electron detector and 10 eV Schottky field emission gun. The instrument is also equipped with an energy-dispersive spectroscopy (EDS) spectrometer (detector from EDAX and software/electronics from Iridium Ultra software iXRF) to characterize the chemical composition. Transmission electron microscopy (TEM) and high-resolution TEM (HRTEM) were performed using a JEM-2100 F instrument. The X-ray diffraction (XRD) patterns were measured using an XRD spectrometer (Rigaku Smartlab) with CuK_α radiation, operated at 45 kV and 200 mA with a scanning rate of 5°/min. The X-ray photoelectron spectroscopy (XPS) data were obtained with an ESCALAB 250Xi electron spectrometer (Thermo Fisher Scientific). The binding energy scale for calibration was carried out using the C1s peak, corresponding to 284.8 eV. Thermal gravimetric analysis (TGA) was conducted on a TGA Q50 instrument from 25 °C to 700 °C at a heating rate of 10 °C/min under the N_2 atmosphere. The zeta potential was determined using a Zetasizer Nano-ZS instrument (Malvern Instruments Ltd) at room temperature. The N_2 adsorption-desorption experiments were performed on an Autosorb iQ Station 1 Analyzer, using the sample degassed at 60 °C for 12 h, where the sample porosity and specific surface area could be determined. The specific surface area was calculated using the BET equation. The pore size distribution was calculated according to the BJH formula. Fourier transform infrared (FTIR) spectra were measured using a T27-Hyperion-Vector22 instrument (Bruker).

UV-vis diffuse reflectance spectra (DRS) were obtained using a spectrophotometer (Varian Cary 5000, USA) with an integrating sphere attachment, where $BaSO_4$ as a reference material. In this experiment, samples of P25 and TiO_2/CNC nanocomposites adsorbed with Cr(VI) (denoted as P25-Cr(VI) and TiO_2/CNC-Cr(VI)) were prepared as follows. A desired amount of P25 or TiO_2/CNC powder samples was added to an aqueous solution of 10 mg/L of Cr(VI) under stirring, where the adsorption process was conducted in dark over night. The suspension was then filtered and the collected solids were dried at room temperature. The resultant P25-Cr(VI) and TiO_2/CNC-Cr(VI), together with TiO_2/CNC, P25 and CNC were also tested to obtain their DRS. Photoluminescence (PL) spectra of solid samples were measured on a Hitachi F-7000 fluorescence spectrophotometer with excitation of the 320 nm wavelength. The electrochemical impedance spectroscopy (EIS) was conducted on an electrochemical workstation (Autolab PGSTAT302 N, Metrohm, Switzerland) using a three-electrode cell with 0.1 M Na_2SO_4 as the electrolyte solution. The working electrode was prepared as following. The prepared samples, PVDF and carbon black (mass ratio of 8:1:1) were mixed with 350 μL DMF to produce a slurry and coated onto indium tin oxide (ITO) glass electrode followed by solvent evaporation.

2.4. Adsorption test

Briefly, 0.06 g catalysts were added to a 60 mL of 10 mg/L Cr(VI) solution, where the pH level was adjusted to 3 using dilute hydrochloric acid. The suspension was stirred for 40 min in dark to reach the adsorption-desorption equilibrium. At each time interval, 2 mL of supernatant was drawn and filtered through a 0.45 μm microporous nylon syringe filter for analysis. The Cr(VI) concentration was determined colorimetrically at 540 nm using the diphenylcarbazide method on a UV–vis spectrophotometer. The concentration of total Cr ions (Cr (T)) was determined via an inductively couple plasma (ICP) spectrometer (ICP-OES, Thermo Scientific), the concentration of Cr(III) in solution was calculated by $C_{Cr(III)} = C_{Cr(T)} - C_{Cr(VI)}$. The adsorption capacity (Q_t) of Cr (VI) was calculated based on the following equation:

$$Q_t = \frac{C_0 - C_t}{m} V \quad (1)$$

where C_0 and C_t stand for the initial Cr(VI) concentration and the Cr(VI) concentration at time t, V is the volume of the solution and m is the mass of the feed catalyst.

2.5. Photocatalytic reduction test

After the adsorption-desorption equilibrium was reached, the photocatalytic reaction was initiated by the visible light using a 300 W Xenon arc lamp with a 420 nm cutoff filter. The applied light intensity was around 300 mW/cm^2. Sample aliquots were drawn periodically and filtered to remove the solid residuals. The Cr(VI) concentration at different time was measured again by the diphenylcarbazide method using the same UV–vis spectrophotometer. Each photocatalytic experiment was measured in triplicate.

3. Results and discussion

3.1. Conception of the TiO_2/CNC synthesis for Cr(VI) photoreduction

Fig. 1 is a schematic illustration of the conception of TiO_2/CNC nanocomposite synthesis and its use for photoreduction of Cr(VI) under visible light. The rationale behind this biotemplate-mediated synthesis approach is as follows. (1) CNC is an effective scaffold to immobilize TiO_2 nanoparticles due to its abundant surface functionalities, good mechanical stability and sustainable nature. (2) The amounts of hydroxyl and sulfuric groups on CNC, serving as a biotemplate to direct the *in situ* growth of TiO_2, can be tailored to control the morphology and crystal structure of TiO_2. (3) The dense nucleation of TiO_2 crystallization on the CNC surface can prevent TiO_2 nanoparticles from agglomerating and CNC from stacking together, which are beneficial for enhancing the high specific surface area. (4) The presence of electron-rich hydroxyl and sulfuric groups on the surface of CNC can induce the formation of ligand-to-metal charge transfer (LMCT) complex, thereby improving the photoreduction activity of converting Cr(VI) into Cr(III) under visible light. This study was carried out based on this conception, and the results are summarized as follows.

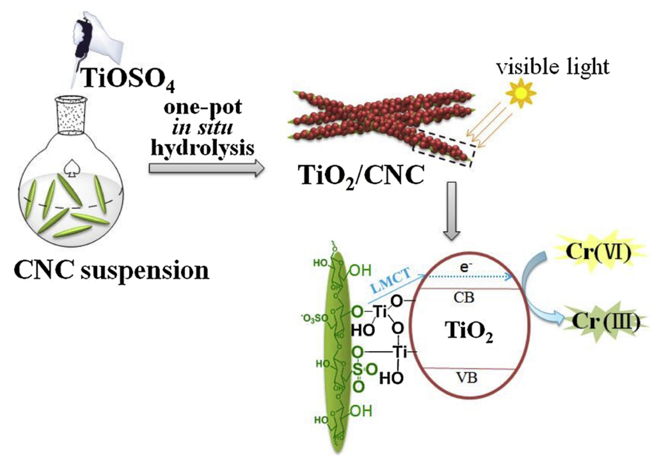

Fig. 1. Schematic illustration of TiO_2/CNC synthesis for photoreduction of Cr (VI).

3.2. Morphology and crystal structure of TiO_2 nanoparticles in TiO_2/CNC nanocomposites

The TiO_2 morphology and the total content in TiO_2/CNC nanocomposites are strongly dependent on the synthetic conditions, including temperature, reaction time and CNC concentration. The results are summarized in Table S1. It was seen that at 70 °C, when the CNC concentration was 0.1 wt% (or below), a large amount of uniform TiO_2 nanocrystals (with diameter < 10 nm) could be formed on the CNC surface, exhibiting a necklace-like structure with no aggregated clusters could be identified under the reaction up to 3 h (Fig. 2). The distribution of TiO_2 on CNC was confirmed by energy dispersive atomic X-ray (EDAX) mapping (Fig. 2g), where indicated that the element of Ti was uniformly distributed in the entire TiO_2/CNC composite. Representative SEM images of TiO_2/CNC nanocomposites obtained by using 0.1 wt% CNC concentration at 70 °C at different reaction times are shown in Fig. 2b–f, where Fig. 2a is the pure CNC scaffold without the synthesis of TiO_2. The pristine CNC image (Fig. 2a) indicates that without TiO_2, the scaffold was film-like with strong aggregation tendency between CNC, where no individual CNC particles or clear CNC bundles could be identified. However, with the inclusion of TiO_2, the overall morphology of the CNC scaffold became more fibrous like, with

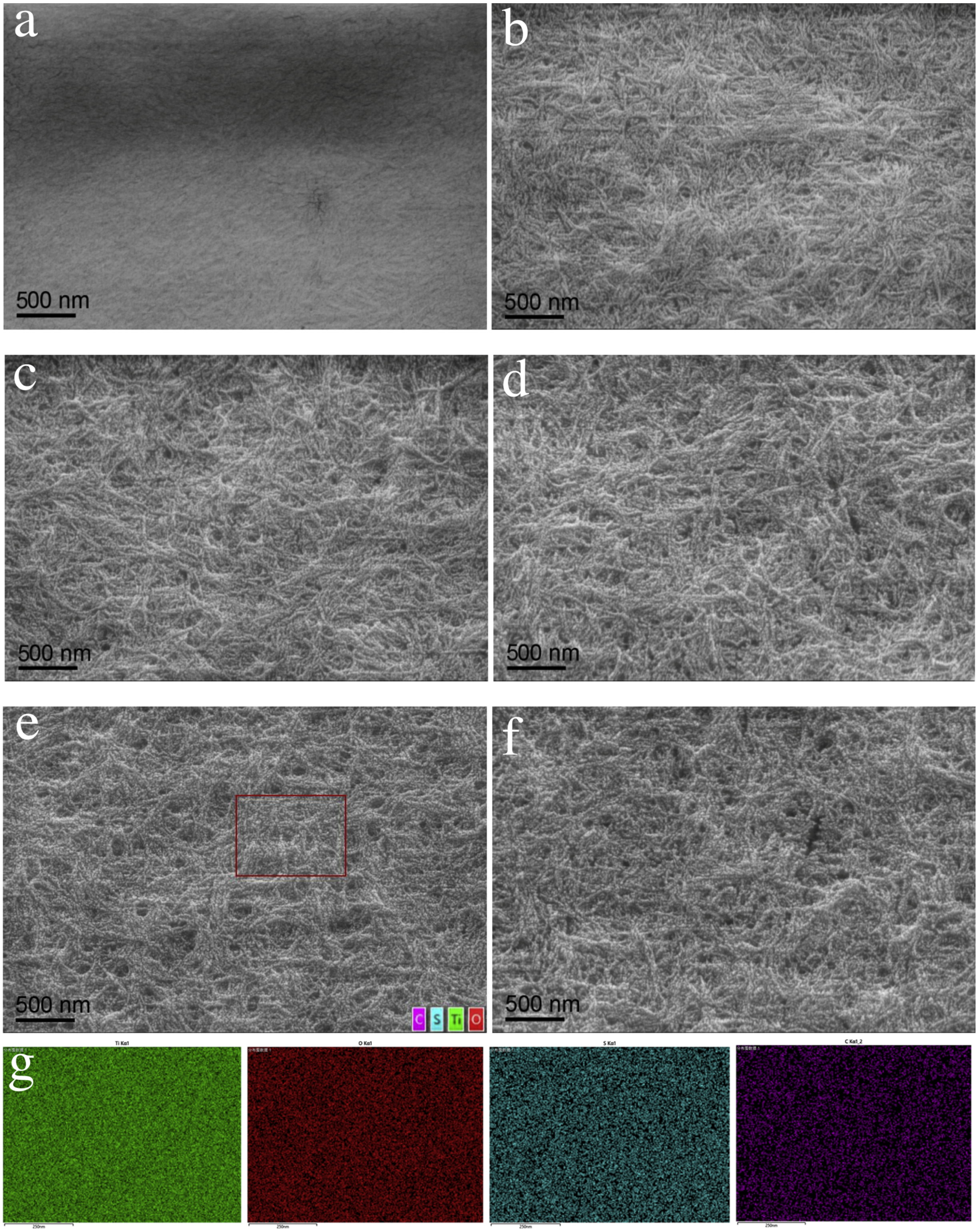

Fig. 2. SEM images of TiO_2/CNC obtained at different reaction times (0.1 wt% CNC concentration, 70 °C): (a) 0 min (pure CNC), (b) 20 min, (c) 40 min (d) 1 h, (e) 2 h, (f) 3 h, (g) EDAX mapping of TiO_2/CNC-2 h (green – Ti; red – O; blue – S; purple – C) (For interpretation of the references to colour in this figure legend, the reader is referred to the web version of this article).

each CNC fibril decorated with TiO_2 nanoparticles clearly apparent in the image. With the increase of the reaction time, the total content of TiO_2 increased (Table S1 in *Supporting Information*).

In Table S1 (*Supporting Information*), the TiO_2 content was seen to increase with reaction time (with 0.1 wt% CNC). Based on the TGA data (Fig. 3a), the nanocomposite synthesized using the 0.1 wt% CNC concentration suspension was found to reach a plateau value (TiO_2 content ~ 33.0 wt%) at 2 h of reaction. When the CNC concentration was equal to or below 0.2 wt%, the chosen synthetic conditions consistently produced uniform TiO_2 nanocrystals. We believe the crystal size increased with the reaction time based on the results on TiO_2 content. However, when the CNC concentration was increased to 0.4 wt

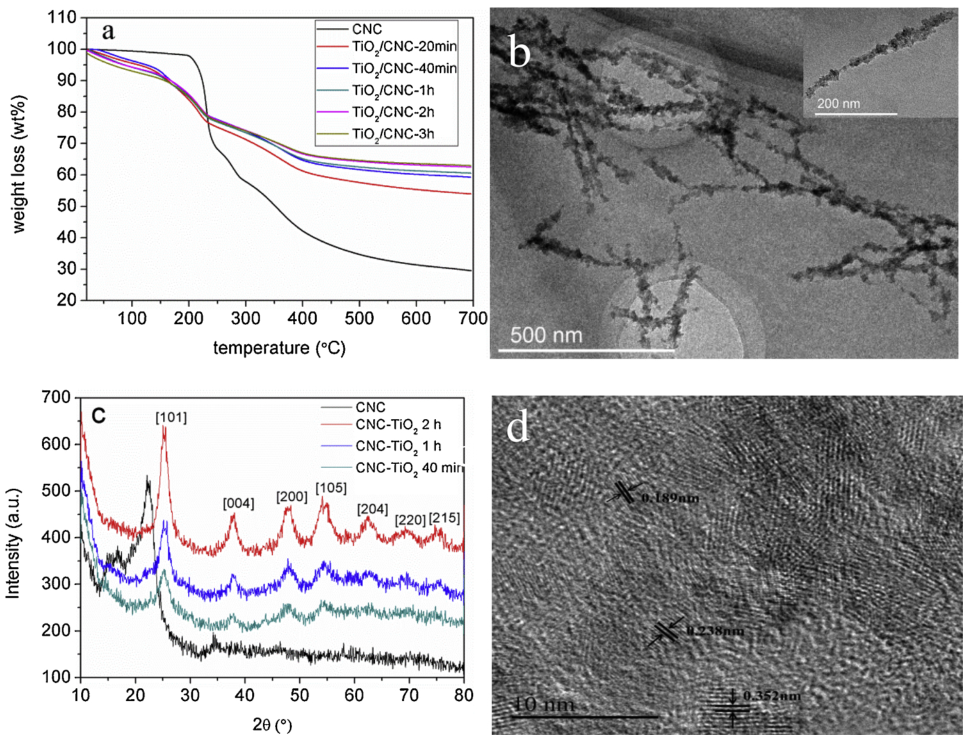

Fig. 3. (a) TGA curves of TiO_2/CNC samples prepared at different reaction times, (b) TEM of TiO_2/CNC-2 h (reaction temperature =70 °C, reaction time =2 h and CNC concentration =0.1 wt%), (c) XRD patterns of TiO_2/CNC samples prepared at different reaction times, (d) HRTEM images of the TiO_2/CNC nanocomposite in (b).

%, the TiO_2 nanocrystals in the CNC scaffold appeared to aggregate together. This is seen in Fig. S2 (*Supporting Information*), where the necklace-shaped fibrillar feature could no longer be discerned. The effect of the reaction temperature (from 50 − 80 °C) on the resulting morphology of TiO_2/CNC nanocomposites was also investigated. It was found that the yield of TiO_2 nanocrystals at the fixed reaction time increased with the reaction temperature. At 50 °C, uniform TiO_2 nanocrystals could still be formed (Fig. S3, *Supporting Information*), but the yield of TiO_2 nanocrystals was very low. According to the results in TGA and SEM, the optimum synthetic conditions for producing the TiO_2/CNC nanocomposite with very uniform TiO_2 nanocrystals were: reaction temperature =70 °C, reaction time =2 h and CNC concentration =0.1 wt%. We denoted the corresponding composite as TiO_2/CNC-2 h in this work. The characterization results of this nanocomposite are as follows.

The successful immobilization of TiO_2 nanocrystals in the CNC scaffold of the TiO_2/CNC-2 h was confirmed by TEM imaging. A TEM image of the stained pristine CNC sample is shown in Fig S1a (*Supporting Information*), and that of the TiO_2/CNC sample without being stained was shown in Fig. 3b. It was seen that the surface of CNC was decorated by TiO_2 nanocrystals quite uniformly. Due to the presence of CNC, it is hard to observe the particles distinctly by TEM, even at high magnification (Fig S4a, *Supporting Information*). In order to determine the TiO_2 size more clearly, CNC was removed by calcined at 500 °C in air, and the mean TiO_2 size was found to be 8.9 nm (Fig S4b, *Supporting Information*). The presence of TiO_2 was further confirmed by the characterization of FTIR and XPS (Fig. S5, *Supporting Information*).

The phase and the crystal structure of TiO_2 were determined by the XRD measurement. Fig. 3c illustrates the XRD pattern of the pristine CNC sample and TiO_2/CNC samples prepared at different reaction times. The diffraction peaks of pristine CNC at 2θ = 14.8°, 16.4° and 22.5°, could be attributed to the [1$\bar{1}$0], [110] and [200] crystallographic planes of the cellulose crystal. TiO_2/CNC samples exhibited additional diffraction peaks at 2θ = 25.3°, 37.8°, 47.8°, 54.1°, 62.5°, 69.2° and 74.7°, which could be attributed to the [101], [004], [200], [105], [204], [220] and [215] crystal planes of the TiO_2 anatase phase. It was noted that the diffraction intensity increased with increasing reaction time, indicating that nanocrystals became perfected. The crystalline size (D) of TiO_2 at 2 h was calculated to be 8.2 nm according to Debye-Scherrer equation, which is slightly smaller than that of the bare TiO_2 determined by TEM:

$$D= \frac{k\lambda}{\beta \cos\theta} \tag{2}$$

where k is a constant equal to 0.89, λ is the wavelength of the X-ray applied (0.154 nm),β is the full width at half maximum of the anatase (101) peak, and θ is the Bragg angle.

The HRTEM image of the TiO_2/CNC-2 h sample is shown in Fig. 3d. In this figure, the crystalline fringe spacings of 0.352 nm, 0.238 nm and 0.189 nm, corresponding to the (101), (004) and (200) facets of the anatase phase of TiO_2, could be clearly identified. These findings are consistent with the XRD results.

3.3. The roles of CNC in the TiO_2/CNC synthesis

It was reported in our previous work that the hydroxyl groups on cellulose could direct the nucleation and growth of TiO_2 nanocrystals. (Li, Cao et al., 2015) This may also be true with CNC. However, CNC contains both hydroxyl and sulfuric groups on the surface, where the effect of the sulfuric groups on the formation of TiO_2 is not clear. To understand the roles of nanocellulose with different functionalities, the following experiments were carried out. First, pristine TiO_2 crystals were prepared without using CNC as a template under the same synthetic conditions as those for TiO_2/CNC, i.e., reaction temperature =70 °C, reaction time =2 h and CNC concentration =0.1 wt%. The result is shown in Fig. 4a, where the formed TiO_2 particles were non-uniform and agglomerate severely (the crystal size could reach the micron scale). In our second experiment, desulfated CNC (*d*-CNC), prepared by acidic treatment, was used as a template in the synthesis of TiO_2/*d*-CNC. This experiment allowed us to assess the role of hydroxyl

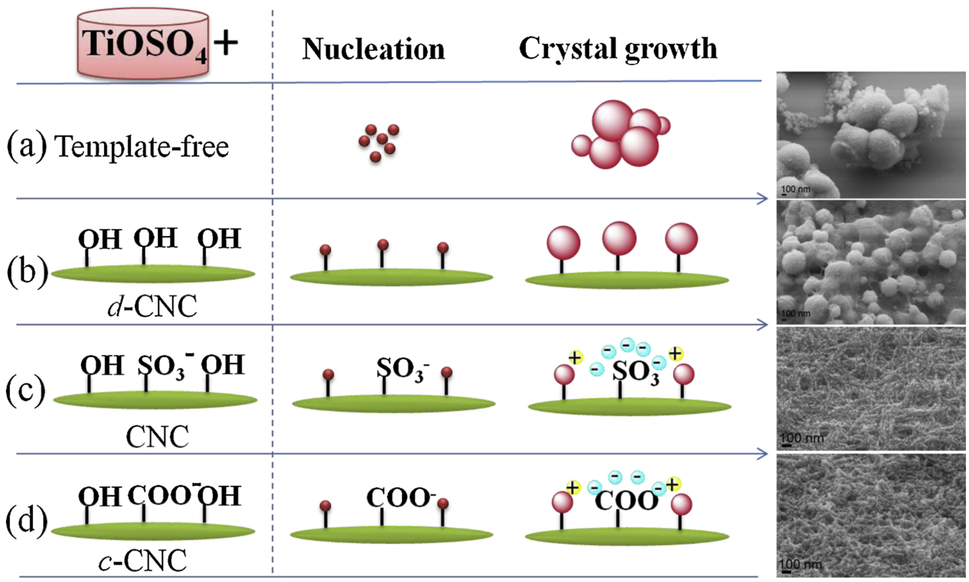

Fig. 4. Schematic presentation of nucleation and growth and the corresponding SEM images of TiO_2 with different templates (a) free of CNC, (b) *d*-CNC, (c) CNC, and (d) *c*-CNC.

groups on the formation of TiO_2 crystals. The result is shown in Fig. 4b, where TiO_2 crystals formed on *d*-CNC possessed a more uniform and smaller size (the average crystal size was about 300 nm) than those synthesized without the CNC template. The above observation positively confirmed the role of hydroxyl groups on *d*-CNC in increasing the nucleation density during the synthesis. In other word, the abundant hydroxyl groups could adsorb Ti^{4+} ions and create nucleating sites on the *d*-CNC surfaces, where the formed nuclei would grow into nanocrystals through condensation reaction. However, the hydrolysis reaction also progressed, breaking some less stable crystals and ripening the more stable crystals. This would result in creating still relatively large TiO_2 crystal size (about 300 nm). This was quite different when the CNC scaffold contains both sulfuric and hydroxyl groups. In the experiment using CNC as a template, a dramatic different TiO_2 crystal size was produced, where the results are illustrated in Fig. 4c. The resulting TiO_2 crystal size was found to be smaller than 10 nm, significantly smaller than those in the scaffold of *d*-CNC. We speculate that the presence of negatively charged sulfuric groups can electrostatically interact with positively charged TiO_2 planes, resulting in the decrease of surface energy and suppressing the size (aggregation) of TiO_2 nanocrystals. To verify the hypothesis of the effect of CNC surface charges on the growth of TiO_2, a *c*-CNC scaffold, containing carboxyl groups instead of sulfuric groups, was used as a template to synthesize the TiO_2/*c*-CNC nanocomposite. The result is shown in Fig. 4d. Again, it was seen that very fine (< 10 nm) and uniform TiO_2 nanocrystals were formed, similar to that of TiO_2/CNC (Fig. 4c). This confirms that the negative charges on the CNC surfaces are essential for the creation of well-distributed nanoscale TiO_2 crystals. As discussed earlier, the hydroxyl groups on the CNC surface can promote and direct the nucleation and growth of TiO_2 crystal. However, in the case of CNC or *c*-CNC, electrostatic interactions can occur between the negatively charged groups (i.e., sulfuric or carboxy groups) and positively-charged TiO_2 and suppress the aggregation of TiO_2 nanocrystals. In addition, the negatively-charged groups can also change the charge distribution in positively-charged $Ti[(H_2O)_6]^{4+}$ hydration ions (the usual existence form of titanium ions in water) and shorten their mean distance, making $Ti[(H_2O)_6]^{4+}$ less stable in the edge connection (i.e., the connection manner of the rutile phase) (Henry, Jolivert, & Livage, 1992; Liu, Wang, Yang, Cheng, & Lu, 2010). Furthermore, the stronger polarity of SO_3^{2-} groups would enable $Ti[(H_2O)_6]^{4+}$ to combine with more hydroxyl groups and form $Ti[(H_2O)_{6-h}(OH)_h]^{4-h}$ during the hydrolysis process, thus in favor of the corner connection (i.e., the connection manner of the anatase phase) through "OH bridge" to form di-oligomers. The di-oligomers can subsequently form three-mentioned networks, resulting the formation of anatase crystal nucleus through the "O-bridge". Finally, the nuclei would grow into anatase TiO_2 through the condensation reaction. It is known that anatase TiO_2 usually exhibits superior photoactivity due to the low packing density, wide band gap, long charge-carrier lifetime, high charge-carrier mobility, and high degree of free hydroxyl radical production. (Kim, Tachikawa, Moon, Majima, & Choi, 2014; Odling & Robertson, 2015)

3.4. BET analysis of TiO_2/CNC nanocomposite

It is well known that nanoparticles have high specific surface area and are prone to aggregate. This possibility was evaluated by the BET analysis to characterize the specific surface area of the chosen TiO_2/CNC-2 h sample. The BET results of pure CNC, P25 and TiO_2/CNC samples are shown in Fig. 5 (Fig. 5a is the N_2 adsorption-desorption isotherms and Fig. 5b is the pore size distributions of CNC, P25 and TiO_2/CNC). Based on the BET analysis measurements, the surface area of CNC was found to be 1.3 m^2/g and that of P25 was 48.6 m^2/g. These values indicated that both CNC and P25 had very low porosity as the measured surface area was much lower than the calculated value, as a result of the particle aggregation and packed structure.(Barringer & Bowen, 1985; Wu et al., 2016) In contrast, the TiO_2/CNC nanocomposite showed a much higher surface area of 112.7 m^2/g, indicating that the presence of TiO_2 nanocrystals greatly hindered the stacking of CNC particles. Compared with CNC and P25, TiO_2/CNC exhibited a type-IV nitrogen adsorption isotherm with a typical H3 hysteresis loop (Fig. 5a), indicating the presence of mesoporous structure. The plot of the pore size distribution (Fig. 5b) was determined using the BJH method from the desorption curve of the isotherm (Fig. 5a). The average pore size of TiO_2/CNC was calculated to be 12 nm. Such a mesoporous structure is extremely beneficial for photocatalysis, as it can shorten the bulk diffusion length of charge carriers and provide flexible transport pathways for the diffusion of reactants during the photocatalytic process. (Chen et al., 2016; Mohamed et al., 2016).

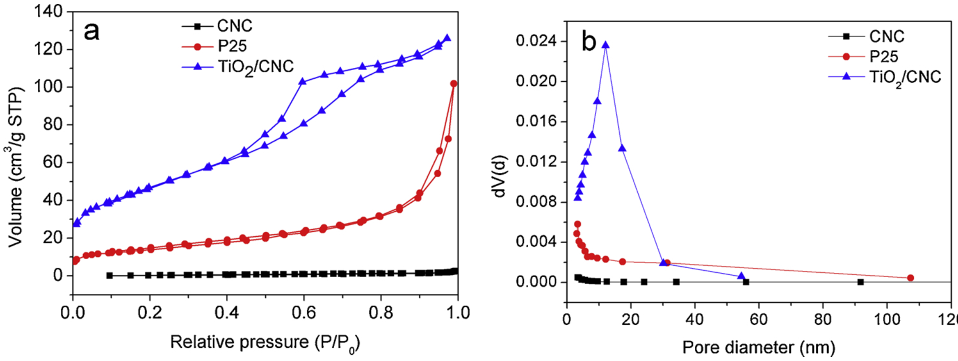

Fig. 5. (a) N_2 adsorption-desorption isotherms and (b) pore size distribution of CNC, P25 and TiO_2/CNC.

3.5. Adsorption and photoreduction of Cr(VI) with TiO_2/CNC

In the previous studies, wet-synthesized TiO_2 was either calcined at high temperatures or hydrothermally treated in order to increase its crystallinity for photocatalysis.(Li & Huang, 2016; Mamaghani, Haghighat, & Lee, 2019) In this study, we demonstrated a low temperature and non-pressurized new pathway to synthesize TiO_2/CNC nanocomposite for photocatalysis. The direct usage of the TiO_2/CNC-2 h nanocomposite for Cr(VI) photoreduction has been carried out, and the results are as follows.

The adsorption test was first conducted in dark to reach an equilibrium state before the initiation of photocatalytic reaction. The results are illustrated in Fig. 6 using the following conditions $[Cr(VI)]_0$ = 10 mg/L, pH = 3, $[TiO_2/CNC]$ = 1.0 g/L. In Fig. 6a, it was seen that TiO_2/CNC adsorbed Cr(VI) rapidly in the first 10 min, and reaches an equilibrium adsorption capacity of 6.7 mg/g within 40 min, outperforming the commercial P25 sample. The Cr(VI) removal efficiency of TiO_2/CNC reached 96 % at 80 min after visible light was turned on, also outperformed the 56 % value of P25. In contrast, CNC alone showed almost no adsorption and photoreduction of Cr(VI). The Cr(VI) reduction could be described by a pseudo-first-order kinetics using the simplified Languir-Hinshelwood model (Fig. 6b). In this analysis, when the dosage of catalysts is 1 g/L, the reaction rate constant was calculated to be 0.027 min^{-1} for TiO_2/CNC, which is 9 times higher than that of P25 (0.003 min^{-1}). Considering the low content of TiO_2 (only 33 wt%) in TiO_2/CNC, this direct comparison with the same dosage might not be straightforward to reflect the high-performance of sole TiO_2 hereby prepared. For a fair comparison, we investigated the Cr(VI) removal efficiency with the 3 g/L dosage of TiO_2/CNC, where the amount of TiO_2 was the same as that of P25 with 1 g/L dosage (Fig. 6a). In both cases, the removal efficiency of Cr(VI) increased with the increasing dosage because more active sites became accessible. It was found that Cr(VI) could be removed completely in 80 min with the 3 g/L dosage of TiO_2/CNC, and the corresponding photoreductive rate

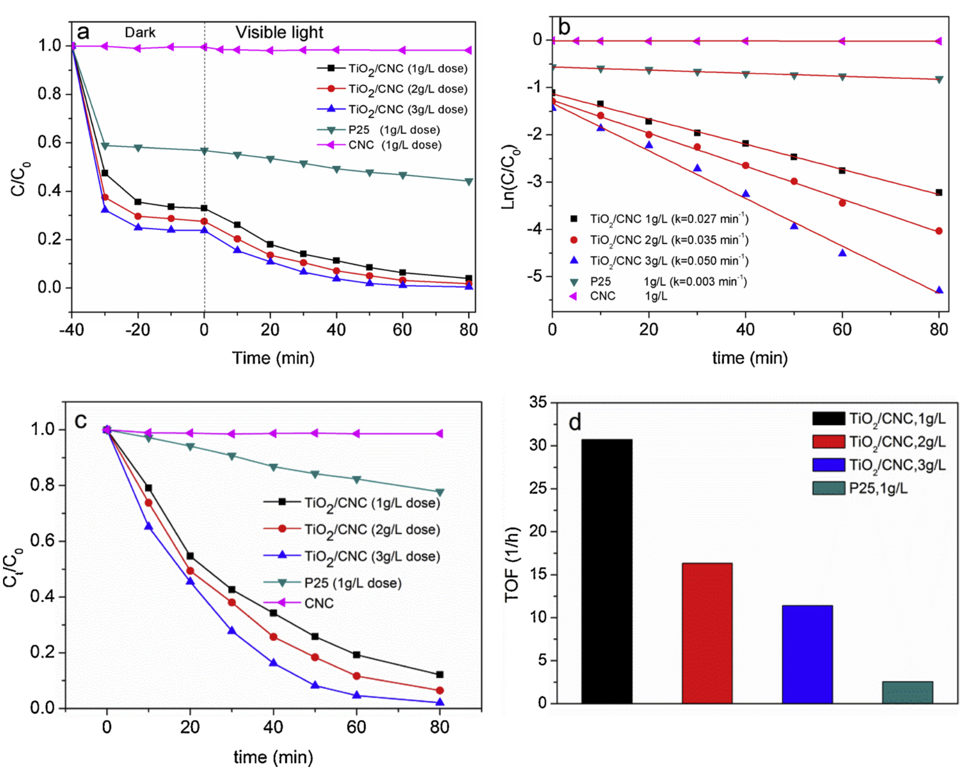

Fig. 6. (a) Adsorption performance of Cr(VI) in dark condition and photoreduction of Cr(VI) under visible light ($[Cr(VI)]_0$ = 10 mg/L, pH = 3), (b) linear kinetic fitting curves of Cr (VI) photoreduction, (c) Photoreduction of Cr (VI) after the adsorption equilibrium. (d) Turnover frequency (TOF) values of samples at varying conditions.

constant was 0.05 min^{-1}, which is 16.7 times that of P25. The turnover frequency (TOF) is one important indicator to access the catalytic activity (v), which was defined as the molar number of reduced Cr(VI) per molar TiO_2 per reaction time ($v = \frac{n_{Cr}}{n_{TiO2}}/t$). As shown in Fig. 6d, the TOF value of TiO_2/CNC was 12 times of P25 with the same catalyst concentration of 1 g/L, and it also outperformed other samples with increasing catalyst concentration.

The higher efficient removal of Cr(VI) by TiO_2/CNC can be attributed to the synergy between adsorption and photoreduction (Li et al., 2016; Wang, Liang et al., 2017). As Cr(VI) was more concentrated on the TiO_2/CNC surface due to adsorption on the large specific surface area in the mesoporous structure, higher degree of reaction involving photogenerated electrons from TiO_2 would take place. In addition, as CNC could remain negatively charged at all pH values (Fig. 7), its surface even in the form of TiO_2/CNC nanocomposite could effectively adsorb positively charged Cr(III) generated from the photoreduction process, as shown in Fig. S6 (*Supporting Information*). As a result, the Cr (III) adsorption increased with the progress of photoreduction. As a result, more active sites on TiO_2 could be refreshed for continuous Cr (VI) reduction, thus promoting the photocatalysis efficiency. Moreover, the smaller TiO_2 crystal size (8.2 nm vs. 21 nm for P25) could shorten the diffusion time of electron transfer from the inside of the particle to its surface, which would also reduce the probability of electron/hole recombination, therefore resulting in the further improvement of photocatalytic activity. (Sheng et al., 2019).

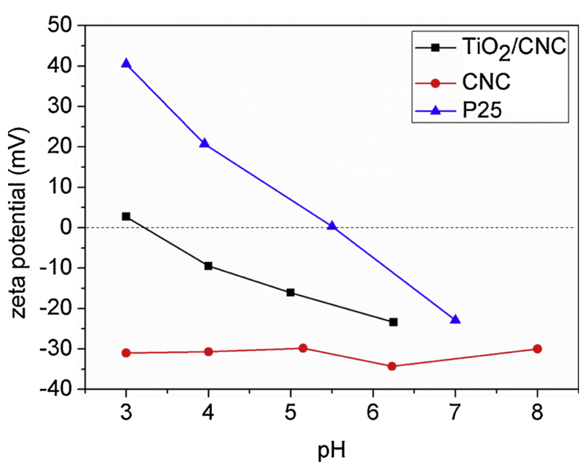

Fig. 7. Zeta potentials of CNC, P25 and TiO_2/CNC samples at different pH values.

To demonstrate the stability and reusability of the TiO_2/CNC nanocomposite system, cycling runs of the photocatalytic reduction of Cr (VI) were evaluated under visible light. After each run, the catalyst was isolated by centrifuging followed by another run without desorption. As shown in Fig. 8, the catalysts can maintain more than 90 % Cr(VI)

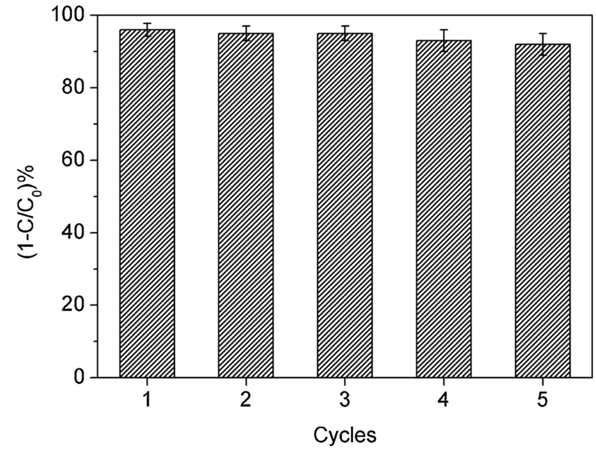

Fig. 8. Cycling runs in the photoreduction of Cr (VI) in the presence of TiO_2/CNC without desorption.

removal efficiency without significant decrease of photocatalytic activity after 5 cycles, suggesting that the adsorption sites can be regenerated by the light irradiation. These results indicate that the demonstrated system has good stability and recycled usability.

3.6. Proposed mechanism for visible-light-driven photoreduction by TiO_2/CNC

It is very interesting to note that the TiO_2/CNC nanocomposite could work as an effective photocatalyst under visible light, given the fact that a much smaller amount of TiO_2 was used in the nanocomposite (33 wt%) as compared with the commercial P25 sample. The interactions between TiO_2 and CNC were investigated using the UV–vis DRS technique (Fig. 9a). The results indicated that both pure P25 and CNC samples showed no visible light absorption, however, TiO_2/CNC exhibited some level of visible light absorption, as evidenced by the red shift of the peak wavelength. Such a shift can be attributed to the formation of the LMCT complex between electron-rich CNC and TiO_2. We speculate that the visible light illumination can induce intramolecular electron transfer from the electron-rich hydroxyl and/or sulfuric groups of CNC to TiO_2. In this case, the electrons are delivered to the adsorbed Cr(VI) ions that consequently enhances the reduction efficiency (illustrated in Fig. 1). The red shift is further confirmed by the noticeable and strong visible light absorption around 600 nm in the TiO_2/CNC-Cr (VI) ternary system, which implies that the existence of Cr(VI) synergistically enhances the absorption of visible light (Yang et al., 2016). Generally, the red shift of light absorption suggests a decrease in the band gap. The corresponding band gap values of P25 and TiO_2/CNC were obtained by plotting the Kubelka-Munk function against the photon energy (Fig. 9b). In this figure, the band gap energy value of TiO_2/CNC was found to be 3.05 eV, smaller than that of P25 (3.25 eV). This confirmed the enhanced light utilization efficiency of the TiO_2/CNC nanocomposite.

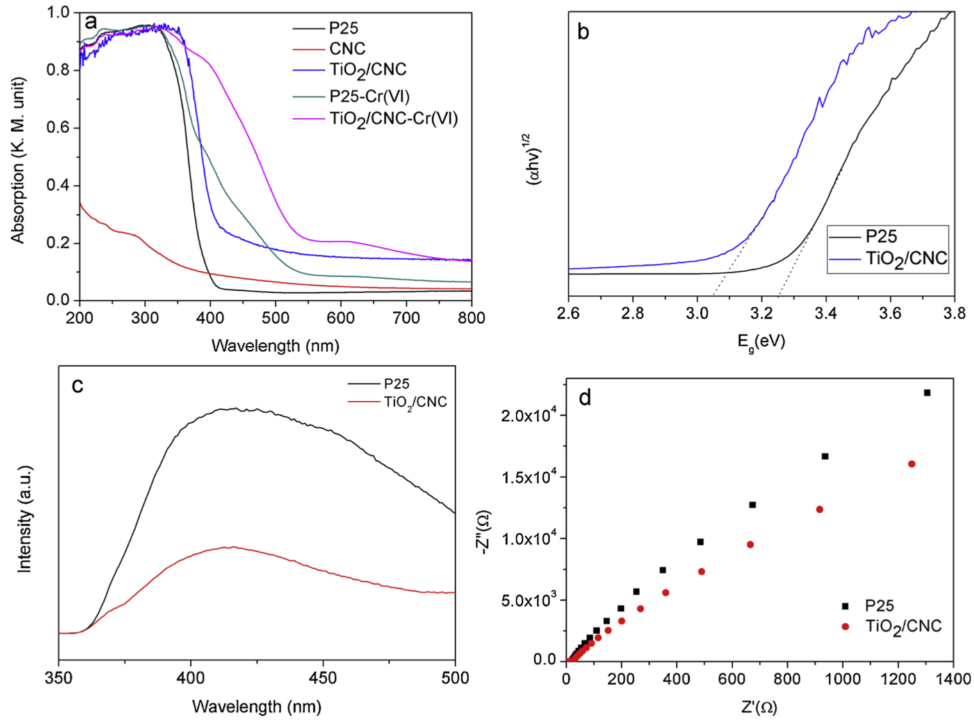

Fig. 9. (a) UV–vis DRS spectra, (b) band gap energy values, (c) photoluminescence (PL) spectra and (d) electrochemical impedance spectra (EIS) of TiO_2/CNC and P25.

We argue that the electron-rich CNC interacted with TiO_2 and formed a LMCT complex, which showed visible light absorption as evidenced by UV–vis DRS analysis. The visible-light-sensitized charge transfer was detected by PL, as shown in Fig. 9c, where the intensity of TiO_2/CNC was found to decrease significantly compared with that of P25. The results indicated that the recombination of photo-generated electron-hole pairs was drastically inhibited, and more long-lived electrons were generated for Cr(VI) reduction. EIS were further carried out to investigate the separation efficiency of the charge carriers. The arc radius of TiO_2/CNC on the EIS Nyquist plot (Fig. 9d) was smaller than that of P25, indicating a lower charge transfer resistance and the more efficient separation of charge carriers. The results from UV–vis DRS, PL and EIS tests provided clear evidence that broader visible light absorption and more efficient charge transfer of electron-hole pairs are probably responsible for the enhanced photoreduction activity of the demonstrated TiO_2/CNC nanocomposite system under visible light (Wang et al., 2010; Zhang et al., 2014).

Based on the experimental results from this study and the schematics in Fig. 1, we can conclude the possible mechanisms of Cr(VI) reduction using TiO_2/CNC nanocomposites, which contain three steps as illustrated in Fig. 10. (1) The formation of a LMCT coordination complex between the charge-enriched CNC and TiO_2, which is accompanied by the appearance of a visible light absorption band, as evidenced by the DRS analysis. (2) The visible light induced charge transfer occurs directly from the ground state of adsorbates (CNC) to the conduction band (CB) of TiO_2, different from the dye-sensitization where the electron must transfer from the excited state of the dyes to TiO_2. thus promoting the efficient separation of charge carriers as evidenced by PL and EIS analysis. (3) The injected electrons excited through LMCT are then delivered to Cr(VI) ions adsorbed on the TiO_2 surface, leading to the photoreduction of Cr(VI) to Cr (III) as described by the following equation (Cr(VI) exists as an anion at the pH level chosen for the adsorption study):

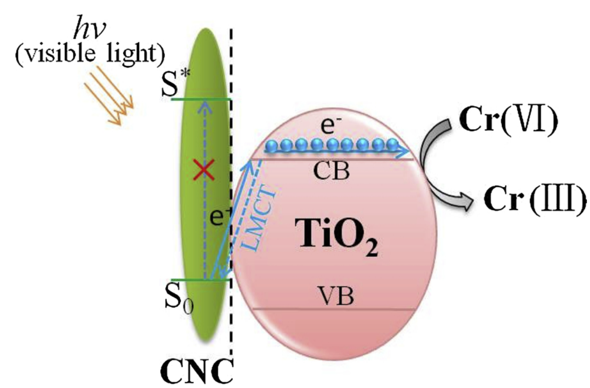

Fig. 10. The proposed photocatalytic mechanism through LMCT on TiO_2/CNC. (S_0 and S* represent the ground state and excited state of the CNC absorbate, respectively).

$$HC_rO_4^{-} + 7H^{+} + 3e- \rightarrow Cr^{3+} + 4H_2O \quad (3)$$

4. Conclusions

We have synthesized TiO_2/CNC nanocomposites through a facile *in situ* hydrolysis method. The TiO_2/CNC composites could be directly used for the photoreduction of Cr(VI) under visible light, and 96 % Cr (VI) was reduced after 80 min irradiation. CNC played two major roles: (1) a biotemplate to direct the crystal growth of TiO_2 and form small sized TiO_2 and uniformed distribution, (2) a LMCT forming ligand to promote the efficient charge transfer of electron-hole pairs in TiO_2. Compared with the widely used hydrothermal method and other wet-synthesis methods that require high-temperature calcination, the demonstrated approach is simple, environmentally friendly, low cost and energy saving. The study provides a new platform for fabrication of efficient TiO_2/CNC-based photocatalysts and enables their applications in water purification.

Acknowledgement

YX Li thanks National Nature Science Foundation of China (21978307) and a Fellowship from the Li Foundation Inc. in USA. The Stony Brook team was supported by a grant from the National Science Foundation in USA (DMR-1808690). The Chinese team was also supported by Key Laboratory of Pulp and Paper Science and Technology by the Ministry of Education and Shandong Province in China (No. KF201722).

Appendix A. Supplementary data

Supplementary material related to this article can be found, in the online version, at doi:https://doi.org/10.1016/j.carbpol.2020.115838.

References

Acharya, R., Naik, B., & Parida, K. (2018). Cr(VI) remediation from aqueous environment through modified-TiO_2-mediated photocatalytic reduction. *Beilstein Journal of Nanotechnology, 9*, 23.

Asahi, R., Morikawa, T., Ohwaki, T., Aoki, K., & Taga, Y. (2001). Visible-light photocatalysis in nitrogen-doped titanium oxides. *Science, 293*(5528), 269–271.

Barrera-Díaz, C. E., Lugo-Lugo, V., & Bilyeu, B. (2012). A review of chemical, electrochemical and biological methods for aqueous Cr(VI) reduction. *Journal of Hazardous Materials, 223–224*, 1–12.

Barringer, E. A., & Bowen, H. K. (1985). High-purity, monodisperse TiO_2 powders by hydrolysis of titanium tetraethoxide. 1. Synthesis and physical properties. *Langmuir, 1*(4), 414–420.

Chen, X., & Mao, S. S. (2007). Titanium dioxide nanomaterials: Synthesis, properties, modifications, and applications. *Chemical Reviews, 107*(7), 2891–2959.

Chen, Y., Li, W. Z., Wang, J. Y., Gan, Y. L., Liu, L., & Ju, M. T. (2016). Microwave-assisted ionic liquid synthesis of Ti^{3+} self-doped TiO_2 hollow nanocrystals with enhanced visible-light photoactivity. *Applied Catalysis B-Environmental, 191*, 94–105.

Cherhal, F., Cousin, F., & Capron, I. (2015). Influence of charge density and ionic strength on the aggregation process of cellulose nanocrystals in aqueous suspension, as revealed by small-angle neutron scattering. *Langmuir, 31*(20), 5596–5602.

Grishkewich, N., Mohammed, N., Tang, J. T., & Tam, K. C. (2017). Recent advances in the application of cellulose nanocrystals. *Current Opinion in Colloid & Interface Science, 29*, 32–45.

Guo, J., Filpponen, I., Johansson, L.-S., Mohammadi, P., Latikka, M., Linder, M. B., et al. (2017). Complexes of magnetic nanoparticles with cellulose nanocrystals as regenerable, highly efficient, and selective platform for protein separation. *Biomacromolecules, 18*(3), 898–905.

Henry, M., Jolivert, J. P., & Livage, J. (1992). Aqueous chemistry of metal cations: Hydrolysis, condensation, and complextion. *Structure and Bonding, 77*, 155–206.

Ivanova, A., Fattakhova-Rohlfing, D., Kayaalp, B. E., Rathouský, J., & Bein, T. (2014). Tailoring the morphology of mesoporous titania thin films through biotemplating with nanocrystalline cellulose. *Journal of the American Chemical Society, 136*, 5930–5937.

Kalashnikova, I., Bizot, H., Cathala, B., & Capron, I. (2012). Modulation of cellulose nanocrystals amphiphilic properties to stabilize Oil/Water interface. *Biomacromolecules, 13*(1), 267–275.

Kaushik, M., & Moores, A. (2016). Review: Nanocelluloses as versatile supports for metal nanoparticles and their applications in catalysis. *Green Chemistry, 18*(3), 622–637.

Kazemi, M., Jahanshahi, M., & Peyravi, M. (2018). Chitosan-sodium alginate multilayer membrane developed by $Fe_0@WO_3$ nanoparticles: Photocatalytic removal of hexavalent chromium. *Carbohydrate Polymers, 198*, 164–174.

Kim, G., Lee, S. H., & Choi, W. (2015). Glucose-TiO_2 charge transfer complex-mediated photocatalysis under visible light. *Applied Catalysis B-Environmental, 162*, 463–469.

Kim, S., Moon, G. H., Kim, G., Kang, U., Park, H., & Choi, W. (2017). TiO_2 complexed with dopamine-derived polymers and the visible light photocatalytic activities for water pollutants. *Journal of Catalysis, 346*, 92–100.

Kim, W., Tachikawa, T., Moon, G. H., Majima, T., & Choi, W. (2014). Molecularlevel understanding of the photocatalytic activity difference between anatase and rutile nanoparticles. *Angew. Chem., Int. Ed. 53*, 14036–14041.

Klemm, D., Kramer, F., Moritz, S., Lindstrom, T., Ankerfors, M., Gray, D., et al. (2011). Nanocelluloses: A new family of nature-based materials. *Angewandte Chemie (International Ed in English), 50*(24), 5438–5466.

Li, L., Li, Y., Cao, L., & Yang, C. (2015). Enhanced chromium (VI) adsorption using nanosized chitosan fibers tailored by electrospinning. *Carbohydrate Polymers, 125*, 206–213.

Li, S., & Huang, J. G. (2016). Cellulose-rich nanofiber-based functional nanoarchitectures. *Advanced Materials, 28*(6), 1143–1158.

Li, Y., Cao, L., Li, L., & Yang, C. (2015). In situ growing directional spindle TiO_2 nanocrystals on cellulose fibers for enhanced $Pb^{(2+)}$ adsorption from water. *Journal of Hazardous Materials, 289*, 140–148.

Li, Y., Cui, W. Q., Liu, L., Zong, R. L., Yao, W. Q., Liang, Y. H., et al. (2016). Removal of Cr (VI) by 3D TiO_2-graphene hydrogel via adsorption enriched with photocatalytic reduction. *Applied Catalysis B-Environmental, 199*, 412–423.

Li, Y. L., Bian, Y. Y., Qin, H. X., Zhang, Y. X., & Bian, Z. F. (2017). Photocatalytic reduction behavior of hexavalent chromium on hydroxyl modified titanium dioxide. *Applied Catalysis B-Environmental, 206*, 293–299.

Liu, G., Wang, L., Yang, H., Cheng, H., & Lu, G. (2010). Titania-based photocatalysts-crystal growth, doping and heterostructuring. *Journal of Materials Chemistry, 20*, 831–843.

Loloei, M., Rezaee, A., Roohaghdam, A. S., & Aliofkhazraei, M. (2017). Conductive microbial cellulose as a novel biocathode for Cr (VI) bioreduction. *Carbohydrate Polymers, 162*, 56–61.

Lu, J., Xu, K., Yang, J., Hao, Y., & Cheng, F. (2017). Nano iron oxide impregnated in chitosan bead as a highly efficient sorbent for Cr(VI) removal from water. *Carbohydrate Polymers, 173*, 28–36.

Makhado, E., Pandey, S., & Ramontja, J. (2019). Microwave-assisted green synthesis of xanthan gum grafted diethylamino ethyl methacrylate: An efficient adsorption of hexavalent chromium. *Carbohydrate Polymers, 222*, 114989.

Mamaghani, A. H., Haghighat, F., & Lee, C. S. (2019). Hydrothermal/solvothermal synthesis and treatment of TiO_2 for photocatalytic degradation of air pollutants: Preparation, characterization, properties, and performance. *Chemosphere, 219*, 804–825.

Mei, J., Zhang, H., Li, Z., & Ou, H. (2019). A novel tetraethylenepentamine crosslinked chitosan oligosaccharide hydrogel for total adsorption of Cr(VI). *Carbohydrate Polymers, 224*, 115154.

Mohamed, M. A., Salleh, W. N. W., Jaafar, J., Ismail, A. F., Abd Mutalib, M., & Jamil, S. M. (2015). Incorporation of N-doped TiO_2 nanorods in regenerated cellulose thin films fabricated from recycled newspaper as a green portable photocatalyst. *Carbohydrate Polymers, 133*, 429–437.

Mohamed, M. A., W. Salleh, W. N., Jaafar, J., Mohd Hir, Z. A., Rosmi, M. S., Abd. Mutalib, M., Ismail, A. F., & Tanemura, M. (2016). Regenerated cellulose membrane as biotemplate for in-situ growth of visible-light driven C-modified mesoporous titania. *Carbohydrate Polymers, 146*, 166–173.

Mondal, S. (2017). Preparation, properties and applications of nanocellulosic materials. *Carbohydrate Polymers, 163*, 301–316.

O'Regan, B., & Grätzel, M. (1991). A low-cost, high-efficiency solar cell based on dye-sensitized colloidal TiO2 films. *Nature, 353*, 737.

Odling, G., & Robertson, N. (2015). Why is anatase a better photocatalyst than rutile? The importance of free hydroxyl radicals. *ChemSusChem, 8*(11), 1838–1840.

Owlad, M., Aroua, M. K., Daud, W. A. W., & Baroutian, S. (2009). Removal of hexavalent chromium-contaminated water and wastewater: A review. *Water, Air, and Soil Pollution, 200*(1), 59–77.

Pelaez, M., Nolan, N. T., Pillai, S. C., Seery, M. K., Falaras, P., Kontos, A. G., et al. (2012). A review on the visible light active titanium dioxide photocatalysts for environmental applications. *Applied Catalysis B, Environmental, 125*, 331–349.

Qu, L. L., Huang, D. L., Shi, H. F., Gu, M. B., Li, J. L., Dong, F., et al. (2015). TiO_2/carboxylate-rich porous carbon: A highly efficient visible-light-driven photocatalyst based on the ligand-to-metal charge transfer (LMCT) process. *The Journal of Physics and Chemistry of Solids, 85*, 173–179.

Sheng, Y. Q., Wei, Z., Miao, H., Yao, W. Q., Li, H. Q., & Zhu, Y. F. (2019). Enhanced organic pollutant photodegradation via adsorption/photocatalysis synergy using a 3D g-C_3N_4/TiO_2 free-separation photocatalyst. *Chemical Engineering Journal, 370*, 287–294.

Tang, J. T., Sisler, J., Grishkewich, N., & Tam, K. C. (2017). Functionalization of cellulose nanocrystals for advanced applications. *Journal of Colloid and Interface Science, 494*, 397–409.

Wang, L., Zhang, C. B., Gao, F., Mailhot, G., & Pan, G. (2017). Algae decorated TiO_2/Ag hybrid nanofiber membrane with enhanced photocatalytic activity for Cr(VI) removal under visible light. *Chemical Engineering Journal, 314*, 622–630.

Wang, N., Zhu, L. H., Deng, K. J., She, Y. B., Yu, Y. M., & Tang, H. Q. (2010). Visible light photocatalytic reduction of Cr(VI) on TiO_2 in situ modified with small molecular weight organic acids. *Applied Catalysis B-Environmental, 95*(3-4), 400–407.

Wang, X., Liang, Y. H., An, W. J., Hu, J. S., Zhu, Y. F., & Cui, W. Q. (2017). Removal of chromium (VI) by a self-regenerating and metal free g-C3N4/graphene hydrogel system via the synergy of adsorption and photo-catalysis under visible light. *Applied Catalysis B-Environmental, 219*, 53–62.

Wu, N., Wei, H., & Zhang, L. (2012). Efficient removal of heavy metal ions with biopolymer template synthesized mesoporous titania beads of hundreds of micrometers size. *Environmental Science & Technology, 46*(1), 419–425.

Wu, X. Y., Shi, Z. Q., Fu, S. D., Chen, J. L., Berry, R. M., & Tam, K. C. (2016). Strategy for synthesizing porous cellulose nanocrystal supported metal nanocatalysts. *ACS Sustainable Chemistry & Engineering, 4*(11), 5929–5935.

Xue, J., Song, F., Yin, X., Zhang, Z., Liu, Y., Wang, X., et al. (2017). Cellulose nanocrystal-templated synthesis of mesoporous TiO_2 with dominantly exposed (001) facets for efficient catalysis. *ACS Sustainable Chem. Eng. 5*, 3721–3725.

Yang, L., Liu, M., Liu, Y., Luo, S., Luo, Y., Luo, X., et al. (2016). Theoretical analyses of organic acids assisted surface-catalyzed reduction of Cr VI on TiO 2 nanowire arrays. *Applied Catalysis B, Environmental, 198*, 508–515.

Zhang, G., Kim, C., & Choi, W. (2017). Poly(4-vinylphenol) as a new stable and metal-free sensitizer of titania for visible light photocatalysis through ligand-to-metal charge transfer process. *Catalysis Today, 281*, 109–116.

Zhang, G., Kim, G., & Choi, W. (2014). Visible light driven photocatalysis mediated via ligand-to-metal charge transfer (LMCT): An alternative approach to solar activation of titania. *Energy & Environmental Science, 7*(3), 954–966.
Zhang, Y. X., Xu, M. J., Li, H., Ge, H., & Bian, Z. F. (2018). The enhanced photoreduction of Cr(VI) to Cr(III) using carbon dots coupled TiO2 mesocrystals. *Applied Catalysis B-Environmental, 226*, 213–219.
Zhao, X., Lv, L., Pan, B. C., Zhang, W. M., Zhang, S. J., & Zhang, Q. X. (2011). Polymer-supported nanocomposites for environmental application: A review. *Chemical Engineering Journal, 170*(2–3), 381–394.
Zhitkovich, A. (2011). Chromium in drinking water: Sources, metabolism, and Cancer risks. *Chemical Research in Toxicology, 24*(10), 1617–1629.
Zhou, Y., Ding, E., & Li, W. (2007). Synthesis of TiO_2 nanocubes induced by cellulose nanocrystal (CNC) at low temperature. *Materials Letters, 61*, 5050–5052.